



Terahertz Electromodulation Spectroscopy for Characterizing Electronic Transport in Organic Semiconductor Thin Films

Philipp Riederer¹ · Roland Kersting¹

Received: 10 October 2022 / Accepted: 29 November 2022 / Published online: 26 December 2022
© The Author(s) 2022

Abstract

Terahertz (THz) spectroscopy is a well-established tool for measuring the high-frequency conductance of inorganic semiconductors. Its application to organic semiconductors, however, is challenging, because of the low carrier mobilities in organic materials, which rarely exceed $10 \text{ cm}^2/\text{Vs}$. Furthermore, low charge carrier densities in organic field-effect devices lead to sheet conductivities that are often far-below the detection limits of conventional THz techniques. In this contribution, we present the application of THz electromodulation spectroscopy for characterizing charge transport in organic semiconductors. Pulses of THz radiation are transmitted through organic field-effect devices and are time-resolved by electro-optic sampling. A differential transmission signal is obtained by modulating the gate voltage of the devices. This controls charge injection into the semiconductors, where the charge carriers reduce the THz transmission by their Drude response. Advantageous is that a nearly noise-free differential transmission can be obtained. Furthermore, electro-modulation allows to sense specifically either injected electrons or holes. Because the method exclusively probes transport of mobile carriers, it provides access to fundamental transport properties, which are difficult to access with conventional characterization methods, such as conductance measurements of organic field-effect transistors. The outstanding property that a relative differential signal is measured allows to obtain charge carrier mobilities with high reliability. Mobilities as small as $1 \text{ cm}^2/\text{Vs}$ can be probed, which makes THz electromodulation spectroscopy an attractive tool for studying charge transport in most technologically relevant organic semiconductors.

Keywords Terahertz spectroscopy · Conductivity · Mobility · Thin films · Organic semiconductors

✉ Roland Kersting
roland.kersting@lmu.de

¹ Photonics and Optoelectronics Group, Faculty of Physics and Center for NanoScience (CeNS), Ludwig-Maximilians-Universität, Königinstr. 10, 80539 Munich, Germany

PACS 07.60.-j · 73.50.-h · 81.70.Fy · 81.05.Fb

1 Introduction and Objective

Many physical properties of semiconductors determine their applicability in future devices, and the corresponding characterization techniques range from conductance measurements to failure analysis [1]. The prime research interest of organic semiconductors focuses on their electrical conductivity. Organic field-effect transistors (FETs) promise application in a variety of fields, ranging from display technology to electrochemical sensing and bioelectronics [2–5]; thus, most works on organic semiconductors investigate charge transport in FETs [6].

Concluding from the devices' conduction onto the physics of charge transport, however, is challenging, particularly when investigating thin films of organic semiconductors, which are polycrystalline by nature. As illustrated in Fig. 1a, contact resistances due to injection and extraction barriers, grain boundaries, and traps slow down charge transport between the source and drain contacts of FETs. Thus, several physical phenomena affect the devices' overall conductance, and the extraction of intrinsic transport properties is difficult and not always unambiguous. The same is expected when using van der Pauw techniques [7, 8], Hall measurements [9, 10], and time-of-flight methods [11, 12], because here, carrier transport is also hindered by grain boundaries and traps. Furthermore, several works have warned that the extraction of the carriers' mobility μ from conductance data have led to severe overestimates in the past [13, 14].

Terahertz (THz) spectroscopy offers an alternative access to intrinsic transport properties of semiconductors [15]. As illustrated in Fig. 1b, charge carriers, as for instance holes, respond to the field $E(t)$ of the incident THz pulse and change the transmission of the THz radiation. By analyzing transmission data in amplitude and phase, the conductivity σ and the Drude mobility μ of the charge carriers

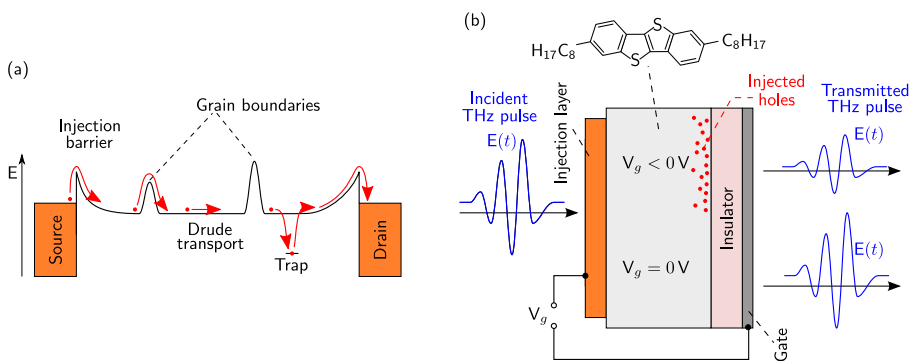


Fig. 1 **a** Illustration of classical conductance measurements. Schottky barriers, grain boundaries, and traps hinder charge transport along the channel between source and drain. **b** Schematic of THz electromodulation spectroscopy where injected charge carriers reduce the transmission of THz radiation

can be deduced. The concept's applicability and precision has been demonstrated in pioneering works on bulk semiconductors, such as silicon and GaAs [16, 17]. However, most technically relevant organic semiconductors are intrinsic and contain no mobile carriers [18]. One technical solution is the photo-generation of electron–hole pairs prior to probing the conductance with THz radiation [19–22]. The separation of the individual conductivities of electrons and holes, however, is difficult, because both affect THz transmission.

In this work, we show that THz electromodulation spectroscopy is a suitable tool for investigating charge transport in molecular semiconductors. As illustrated in Fig. 1, the polarity of the gate voltage causes the injection of either electrons or holes. Thus, only one type of carriers is probed, and switching between two gate voltages V_g provides a differential THz signal, from which the sheet conductivity σ_{2D} and the Drude mobility μ can be deduced. Similar techniques have been developed for the microwave region [23, 24].

2 Experimental Technique

2.1 Setup for THz Electromodulation Spectroscopy

In a semiconductor thin film, the conductivity of the charge carriers causes absorption and dispersion of THz radiation when transmitted through the structure. Insight into the physics of charge transport can be obtained from the frequency dependence of the transmission, and it is common practice to resolve the THz signals in time-domain followed by Fourier transformation of the data [25, 26]. The required sub-picosecond time resolutions can be achieved, for instance, by Auston switches [27], photoconductive antennas [28, 29], homodyne mixing [30, 31], heterodyne mixing [32, 33], and electro-optic sampling [34, 35].

The setup presented here utilizes electro-optic sampling and is illustrated in Fig. 2. The laser source is a Ti:Sapphire oscillator, which produces pulses of 80-fs duration centered at 780 nm at a repetition rate of 80 MHz. A beam splitter divides the laser power into a 500-mW beam for exciting the THz emitter and a sampling beam of 100 mW, which is used for time-resolving the THz signal. The THz emitter is an interdigitated metal-semiconductor-metal structure fabricated on top of semi-insulating GaAs as described in Ref. [36]. For collimating and for focusing the THz radiation, off-axis parabolic mirrors with working distances of 100 mm and 150 mm are used. The sample is positioned at one focus of the THz beam path. For low-temperature measurements, a cryostat can be inserted through a 100-mm flange. The radiation transmitted through the sample is focused onto a 1-mm-thick (110) ZnTe crystal. The probe beam passes a polarizer and a half-wave plate ($\lambda/2$). After reflection on a semi-insulating silicon wafer, the probe beam is brought to overlap with the THz pulses within the ZnTe crystal for electro-optic sampling of the THz field. A Wollaston prism splits up the two polarization components, each of which is detected by a photodiode. This copies the THz pulses' amplitude and phase information onto the 780-nm beam. A quarter-wave plate ($\lambda/4$) is used for balancing the DC current of the photodiodes.

The photodiodes' differential photocurrents are amplified and measured using a digital lock-in amplifier (LIA). As will be shown in Section 3, the signal changes due to the charge carriers are minute and their detection requires efficient noise suppression, which can be achieved by modulating the THz beam at high frequency. In our setup, modulation frequencies of approximately 40 kHz are used for switching the electrical polarity of the THz emitter and thus the polarity of the emitted THz pulses. For this, the LIA's reference output sources a power amplifier, which drives the THz emitter (Em) with an amplitude of 8 V. The AC signal of the photodiodes is amplified by the LIA and averaged by a low-pass filter with a time constant of 30 μ s. The output voltage is digitized at 102 kHz with 24-bit resolution prior to processing by the measurement software.

The absorption of THz radiation by water is eliminated by mounting the optical setup in a vacuum chamber, which reaches pressures of 0.1 mbar. Figure 3 shows typical THz transients obtained without a sample. The data are recorded in dependence on time delay t between THz pulse and sampling laser pulse (illustrated in Fig. 2). The corresponding spectrum spans from approximately 0.3 to 2.6 THz. Because of the setup's insulation by the vacuum chamber and the referencing at 40 kHz, the signal-to-noise ratio of the setup reaches $\eta = 2 \times 10^5 \text{ Hz}^{1/2}$.

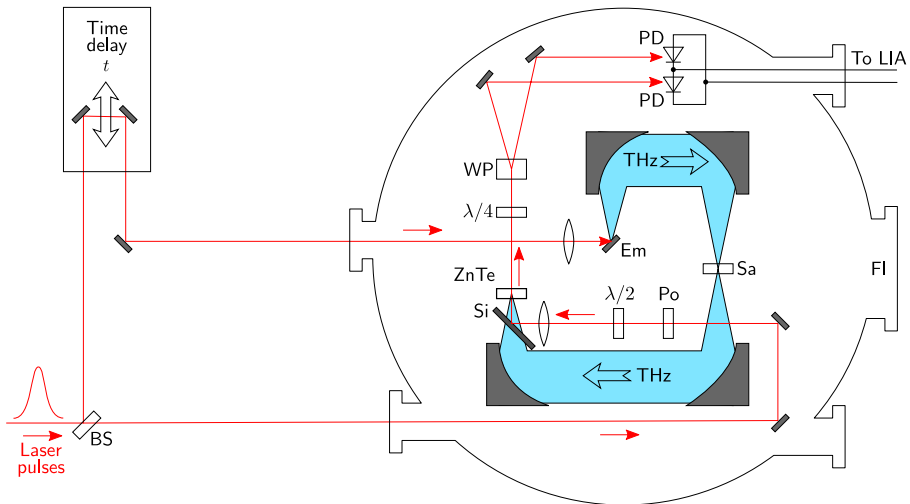


Fig. 2 Schematic of the setup. The vacuum chamber has a diameter of 0.8 m. Abbreviations used: Terahertz emitter (Em), sample (Sa), flange for inserting an optional sample cryostat (FI), beam splitter (BS), polarizer (Po), half-wave plate ($\lambda/2$), quarter-wave plate ($\lambda/4$), silicon beam splitter (Si), zinc telluride crystal (ZnTe), Wollaston prism (WP), photo diode (PD), lock-in amplifier (LIA)

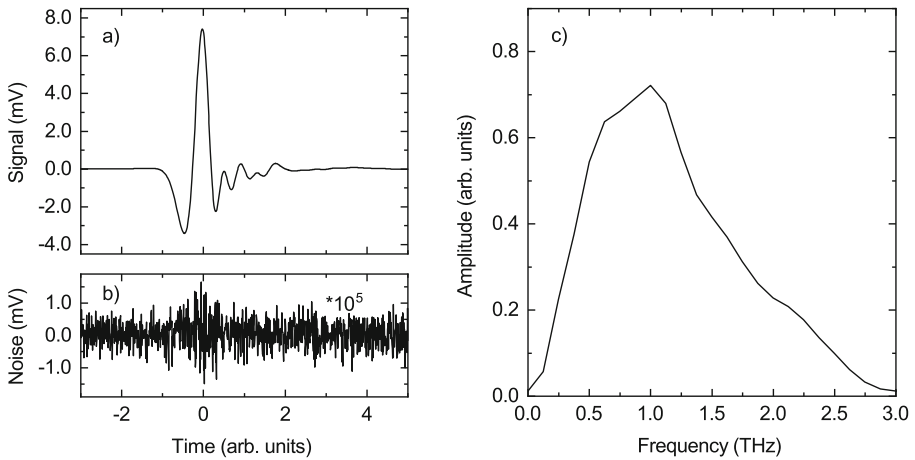


Fig. 3 **a** Time-resolved THz pulse acquired at a total integration time of 20 s per data point. **b** Noise of the system. **c** Corresponding amplitude spectrum

2.2 Thin-Film Devices

The classical approach for deducing the charge carriers' conductivity σ is to compare two THz transients: one recorded after transmission through the semiconductor and a second one, a reference, without the sample [16, 17]. This concept cannot be applied when characterizing organic thin films. Compared to silicon, where electron mobilities can reach $\mu \approx 1500 \text{ cm}^2/\text{Vs}$, the mobilities in organic semiconductors rarely exceed $10 \text{ cm}^2/\text{Vs}$. Furthermore, organic field-effect structures have accumulation layers that are only a few nanometers thick [18, 37]. Both lead to diminutive sheet conductivities $\sigma_{2D} = e\mu n_{2D}$ and thus to a weak interaction between the THz radiation and the carriers within the organic semiconductor. Changes in the setup's performance between two consecutive measurements would cause transmission changes that exceed by far the imprint of the charge carriers onto the THz transmission.

Electromodulation overcomes this challenge. Within milliseconds, charge carriers can be electrically injected into the device or can be extracted. This allows for recording the two required transmission signals without mechanically replacing the sample. The technique, however, requires electrically controllable semiconductor thin films. A suitable device structure is illustrated in Fig. 4a. The geometrical dimensions of the devices are set by the focal width of the THz beam. An active area with a diameter of 5 mm is appropriate for the setup discussed above.

All devices presented here are fabricated on 1-mm-thick sapphire substrates or on $125 \mu\text{m}$ -thick foils of polyethylene naphthalate (PEN). Devices on PEN foil are flexible, as shown in Fig. 4b and allow the fabrication of large sets of individual structures on a single foil. The advantage of sapphire substrates is their good heat conductance, which is required for low-temperature experiments.

The first layer deposited on top of the substrate is a 6-nm-thick chromium film, which will later serve as gate contact. This thin chromium layer sufficiently transmits

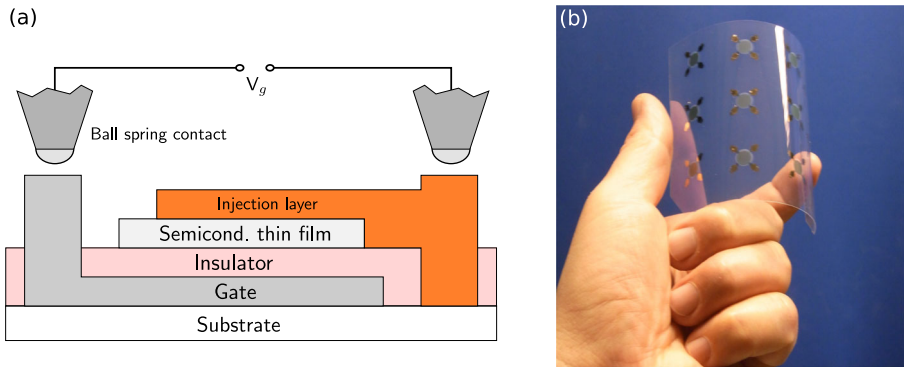


Fig. 4 **a** Schematic of a cross section through a device for THz electromodulation spectroscopy. **b** Image of bendable devices fabricated on PEN foil

THz radiation. The insulator is a parylene N film with a thickness of approximately 300 nm. At this thickness, break-through fields of about 2.5 MV/cm can be reached, which sets the upper limit of the injected charge density to nearly $4 \times 10^{12} \text{ cm}^{-2}$.

The organic semiconductor is deposited on top of the parylene and has a thickness of about 50 nm. This work presents data obtained on the molecular semiconductors dinaphtho[2,3-b:2',3'-f]thieno[3,2-b]thiophene (DNTT) [38], 2,7-dioctyl[1]benzothieno[3,2-b][1]benzothiophene ($\text{C}_8\text{-BTBT-C}_8$), and 2,7-didodecyl[1]benzothieno[3,2-b][1]benzothiophene ($\text{C}_{12}\text{-BTBT-C}_{12}$) [39]. As injection layers, various materials can be used, such as 2 nm Au topped by 6 nm Cr or 3 nm MoO_x followed by 6 nm Cr. The purpose of the chromium is to provide conductivity across the device, whereas the purpose of the gold and MoO_x is to establish electrical contact to the underlying molecular semiconductor. A precise control of the contact metal thicknesses is crucial as layers thinner than 5 nm often show no percolation whereas thick layers reduce the transmitted signal significantly. Additionally, the thickness of the injection metal depends on the roughness of the semiconductor. On rough semiconductors, metal films with thicknesses up to 15 nm may be needed in order to achieve full percolation.

Good electrical contacts require metallic layers with work functions that fit the band edges of the organic semiconductor. The work functions of Au (4.7 eV) and MoO_x (≈ 5.6 eV) are close to the valence bands of many molecular semiconductors, which reduces the height of the injection barriers and allows for efficient injection of holes [40, 41].

The metallic layers and the molecular semiconductors are fabricated by physical vapor deposition at a base pressure of 10^{-7} mbar. Typical deposition rates are 0.2 Å/s. The parylene N layers are fabricated by chemical vapor deposition [42] at a pressure of 10^{-2} mbar with a deposition rate of 1 Å/s. Prior to every deposition step, the devices are heated up to 60°C at 10^{-7} mbar for several hours, which removes residual water and other contaminants from the surfaces and increases the purity of the deposited semiconductors. After fabrication, the devices may be sealed with 300 nm of parylene N (not shown in Fig. 4), which prevents indiffusion of contaminants and increases the device lifetime.

Electrical contact to the devices is achieved by ball spring contacts. The two metal layers that sandwich the semiconductor form a capacitor with a capacitance of $C \approx 2$ nF. Each of the two metal layers has two leads, by which the load resistance of the capacitor can be deduced, which is typically $R \approx 1$ k Ω . The resulting time constant $\tau_{RC} = RC \approx 2$ μ s, sets the upper limit of the modulation frequency of the devices. The experiments shown here are performed at modulation frequencies below 100 Hz.

3 Results on Molecular Thin Films

In molecular semiconductors, conduction due to electrons, as well as due to holes, has been observed [18]. In general, the mobilities in p-conducting materials exceed by far those observed in n-conducting molecular semiconductors [43]. In this work, we focus exclusively on p-conducting molecular semiconductors.

With the injection of charge carriers, the THz transmission ΔS through the devices decreases, as shown in Fig. 5. All investigated devices show relative transmission changes $|\Delta S/S| \leq 2 \times 10^{-4}$. These small signals attest the need for excellent noise properties of the setup. Ramping the gate voltage V_g causes the injection of charge carriers into the semiconductor and thus a reduction of the THz transmission, as shown in Fig. 5. However, the THz signal is reduced only while V_g is negative, that is, during periods when holes are accumulated within the semiconductor. At positive V_g , no reduction of the THz transmission is observed, as it would be expected for electrons. Apparently, the conductance due to the injection of electrons is marginal, which may either be because of too high injection barriers or negligible conductance of the injected electrons.

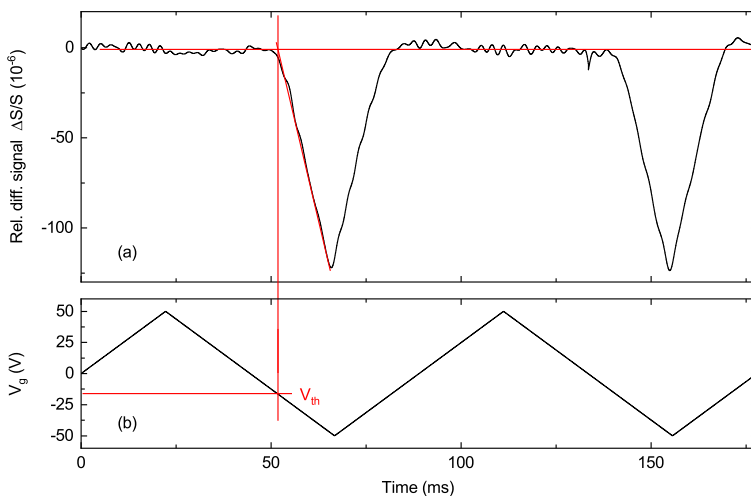


Fig. 5 Electromodulation of a C₈-BTBT-C₈ device on the millisecond time scale. **a** Change of the transmission signal $\Delta S/S$ recorded at the peak of the THz pulse. **b** Applied gate voltage. The red lines illustrate the procedure for deducing the threshold voltage V_{th}

The THz signal in Fig. 5a linearly follows the applied gate voltage as shown in Fig. 5b. Thus, the time delay between application of V_g and the actual charging or discharging of the device occurs on time scales that are much shorter than the modulation period of about 100 ms (Fig. 5). An exponential dependence as it would be expected for significant injection barriers is not observed.

The analysis of the THz signals described in Section 4 requires knowledge of the injected sheet density of charge carriers $n_{2D,inj}$. Two methods can be applied: (i) Measurements of the device's capacitance per unit area \tilde{C} provide a good estimate of the injected charge in dependence of applied gate voltage V_g . Nevertheless, this procedure requires that injection barriers can be neglected and that the charge carrier density follows in a linear manner V_g as indicated in Fig. 5. (ii) Alternatively, the injected density $n_{2D,inj}$ can be deduced by integrating the time-dependent charging current. In all experiments reported here, we find no significant difference between the values determined with the two methods. However, both methods provide only the density of charges injected into the device $n_{2D,inj}$, which is not necessarily identical with the density of mobile charges n_{2D} within the accumulation region at the interface to the insulator.

Figure 5 also shows an offset between V_g and the decay of the THz transmission, the threshold voltage V_{th} . In most devices, V_{th} is negative, and holes are injected only if $V_g < V_{th}$. The linearity of the signal in Fig. 5 suggests that a polarization density P is present within the device and that the sheet density of mobile charge carriers is described by

$$e n_{2D} = \tilde{C} V_g - P \quad (1)$$

where \tilde{C} is the unit capacitance per area. Evaluating the threshold voltage, as indicated in Fig. 5, therefore allows for determining the carrier sheet density n_{2D} . The difference between $n_{2D,inj}$ and n_{2D} results from the built-in polarization of the device. For the following measurements, typical sheet densities of $n_{2D} \approx 10^{12} \text{ cm}^{-2}$ are deduced.

The charge carriers within the device respond in an oscillatory motion to the driving THz pulse, as shown in Fig. 6a by $\Delta S(t)$. The transients are recorded by applying a square-wave voltage with an amplitude of 50 V at a frequency of about 11 Hz. For each modulation state, two signals are recorded: one without charge carriers within the semiconductor and one with carriers, $S_0(t)$ and $S_1(t)$, respectively. The difference $\Delta S(t) = S_1(t) - S_0(t)$ is about four orders of magnitude smaller than the original transmission signals. Between the two modulation states, only the hole density within the device changes. Thus, $\Delta S(t)$ exclusively results from the response of the charge carriers to the THz pulse. A closer inspection proves causality of the charge carrier's response. The magnifications of the center peaks in Fig. 6c and d show that the charge carriers delay the transmission of the THz pulses.

4 Analysis of Electromodulation Data

The purpose of THz electromodulation spectroscopy on thin film semiconductors is to determine electrical properties, such as conductivity σ and mobility μ . A first

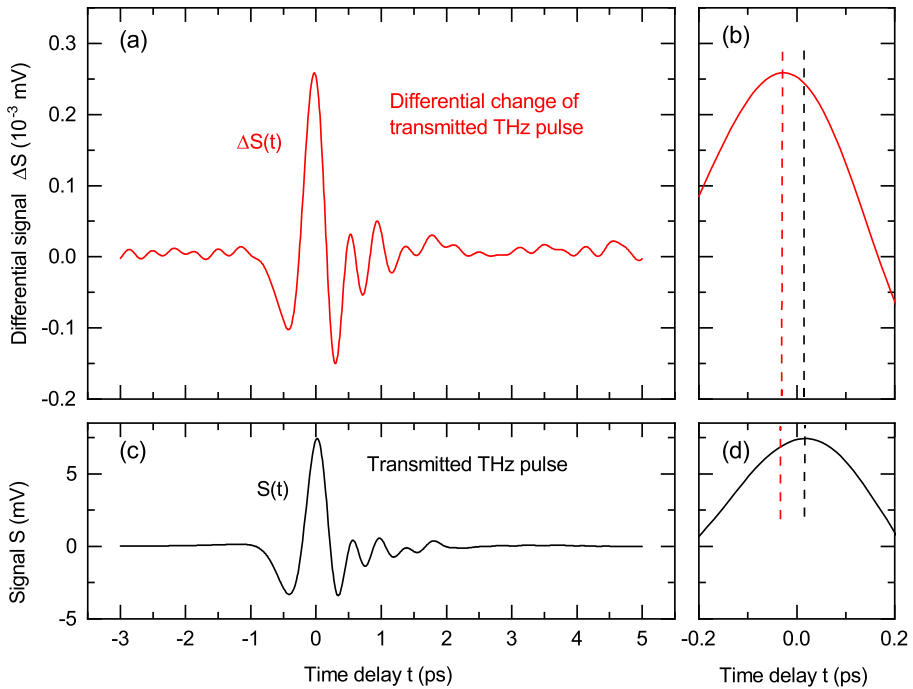


Fig. 6 **a** Transmission change ΔS due to electromodulation of a DNTT device at $V_g = \pm 50$ V. **b** Magnification of the peak of $\Delta S(t)$. **c** Signal $S(t)$ of the transmitted THz pulse and **d** magnification of the peak of $S(t)$

estimate can be drawn from the extremal values of ΔS of the data shown, for instance, in Figs. 5 and 6, using an equivalent of Tinkham’s formula [44, 45]:

$$\sigma_{2D} = \frac{-\Delta S}{S} \frac{2\sqrt{\epsilon_b}}{Z_0} \tag{2}$$

where ϵ_b is the background permittivity of the semiconductor and $Z_0 = 376.7 \Omega$ is the impedance of free space. Supposition of the above approximation is that the thickness of the conducting sheet is much smaller than the wavelength, which is the case in our structures [46]. Taking, for instance, $-\Delta S/S = 10^{-4}$ from Fig. 5 and assuming for $\epsilon_b = 2.8$ [24, 47] yields $\sigma_{2D} = 0.89 \times 10^{-6} \Omega^{-1}$ and $\mu = 2.8 \text{ cm}^2/\text{Vs}$ when using the estimate of Eq. 2.

Such an estimate, however, neglects the frequency dependence of the charge carriers’ response. Previous work [48] has shown that the holes’ response can be well described by Drude gas with complex sheet conductivity:

$$\sigma_{2D}(\omega) = \frac{n_{2D} e^2 \tau}{m_h^*} \cdot \frac{1 + i \omega \tau}{1 + \omega^2 \tau^2} \tag{3}$$

where τ is the Drude scattering time, m_h^* is the holes’ effective mass, and ω is the angular frequency.

The complex conductivity causes not only absorption and dispersion of the transmitted THz radiation. Additionally, reflections may occur at every interface, because the index of refraction of the semiconductor changes with n_{2D} . A rigorous treatment would require calculation of the device’s overall transmission by matrix methods [49]. However, the quantity $\Delta S/S$ is a relative differential signal. This allows for neglecting the optical transmission through the substrate, the gate metal, and the injection layer. For obtaining $\Delta S/S$, two different layer stacks have to be analyzed, as illustrated Fig. 7. Both stacks are the same, except for layer 2, which either contains no charge carriers (a) or the injected charges (b). The thicknesses are $d_1 \approx 300$ nm, $d_2 \approx 3$ nm, and $d_3 \approx 50$ nm.

The propagation of THz radiation through a layer indexed by n is described by its complex wave vector k_n and $E_n(t) = E_{n,0} \exp\{i(k_n z - \omega t)\}$ for the electric field, when assuming propagation in z -direction. In conducting media, the current density is $j = \sigma E$ and the wave vector becomes [50]:

$$k = \sqrt{\omega^2 \epsilon_b \epsilon_0 \mu_0 + i \omega \mu_0 \sigma} \tag{4}$$

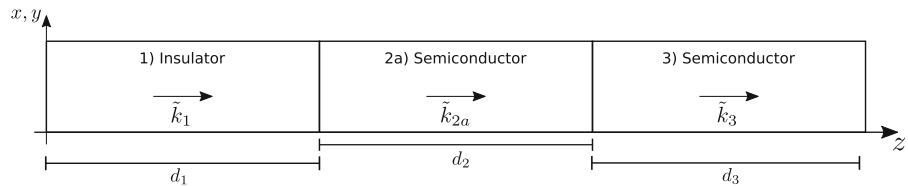
where ϵ_b is the relative background permittivity of the material, and ϵ_0 and μ_0 are the electric and magnetic field constants, respectively.

Considering absorption within the layers and reflection at every interface leads to the complex transmission of such a three-layer system [49]:

$$t = \frac{4 k_1 k_2 e^{i k_2 d_2}}{(k_1 + k_2)(k_2 + k_3) + (k_1 - k_2)(k_2 - k_3) e^{2 i k_2 d_2}} \tag{5}$$

Again, absorption and dispersion within layers 1 and 3 do not need to be considered for evaluating transmission changes due to modulation of layer 2. A similar equation was derived for changes of the index of refraction by photoinjected carriers [51].

(a) Without injected charge carriers



(b) With charge carriers

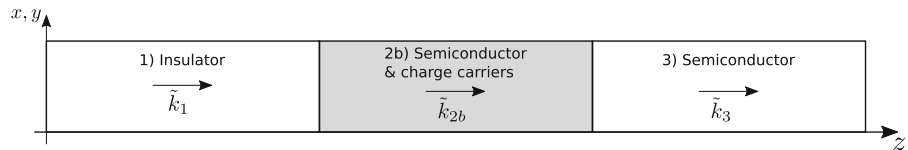


Fig. 7 Layer sequence for analyzing the relative differential transmission $\Delta S/S$. The illustrations visualize the two modulation states: **a** without injected carriers and **b** state with injected carriers. The thicknesses of the layers are d_i and the complex wave vectors of the THz radiation are labelled by k_i

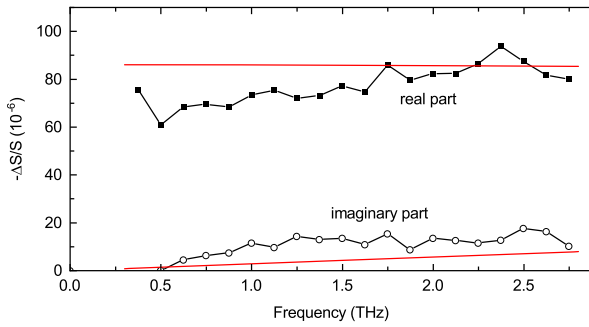


Fig. 8 Relative differential transmission obtained on C_{12} -BTBT- C_{12} in dependence of frequency. The experimental data for the real and imaginary part of the differential transmission are shown by black squares and circles, respectively. Calculations based on the Drude model are shown by red lines. Reprint with permission from Ref [48]. Copyright 2017 American Chemical Society

Using Eq. 5, the calculated relative differential transmission follows from:

$$\frac{\Delta S}{S} = \frac{t_{2b} - t_{2a}}{t_{2a}} \quad (6)$$

where t_{2a} and t_{2b} are the transmissions calculated for the modulation states without carriers and with carriers, respectively.

Experimental data obtained on C_{12} -BTBT- C_{12} and calculated data are compared in Fig. 8 in frequency domain. Measurements, such as those displayed in Fig. 6, provide $\Delta S(t)$ and $S(t)$, which are Fourier-transformed to $\Delta S(\nu)/S(\nu)$. The symbols in Fig. 8 show the real part and the imaginary part. Also shown are calculations following Eqs. 3 to 6. Used parameters are $n_{2D} = 0.92 \times 10^{12} \text{ cm}^{-2}$, which is deduced from the devices unit capacitance using gate voltage $V_g = -50 \text{ V}$ and threshold $V_{th} = -12 \text{ V}$. For the effective hole mass m_h^* , the free electron mass is assumed. This leaves the Drude scattering time τ as a fit parameter. Reasonable agreement between experimental data and calculation is achieved for $\tau = 5.3 \text{ fs}$. The corresponding Drude mobility is $\mu = e\tau/m_h^* = 9.3 \text{ cm}^2/\text{Vs}$. In a similar way, mobilities of $21 \text{ cm}^2/\text{Vs}$ have been deduced for pentacene [52]. For DNTT, $\mu = 1.5 \text{ cm}^2/\text{Vs}$ is deduced by considering the frequency dependence given in Eq. 3, which exceeds the value of $0.84 \text{ cm}^2/\text{Vs}$ obtained with the estimate according to Eq. 2. The origin of the difference shows that considering the frequency dependence goes beyond the estimate of $\Delta S/S$ from the peak amplitude only.

The obtained mobilities are local mobilities and mirror the intrinsic transport properties of the semiconductors investigated. For the holes in the accumulation region, a mean free path $L = \sqrt{2k_B T \tau^2/m_h^*} \approx 0.5 \text{ nm}$ is estimated using the fit parameters of $m_h^* = m_e$ and $\tau = 5.3 \text{ fs}$. This distance is much smaller than the grain sizes, which are about 250 nm . Thus, the majority of the holes is not hindered by grain boundaries when following the THz field in an oscillatory motion. Similar holds for traps, for which a minimum spacing of $d_{\text{trap}} \geq 10 \text{ nm}$ can be deduced from n_{2D} , because apparently, not all holes are trapped. Altogether, THz electromodulation spectroscopy probes the intrinsic mobility of charge carriers on local nanoscopic scale.

5 Limitations of the Technique and Future Applications

One factor that limits the application of the technique is the noise of the setup. The relative noise of every data point can be estimated from the signal-to-noise ratio of the technique η , the number of data points of one scan N_{sampl} , and the scan's integration time T_{tot} :

$$\frac{\Delta y}{y} = \frac{1}{\eta} \sqrt{\frac{T_{\text{tot}}}{2 N_{\text{sampl}}}} = 6.7 \times 10^{-6} \quad (7)$$

when assuming $\eta = 2 \times 10^5 \text{ Hz}^{1/2}$, $N_{\text{sampl}} \approx 1000$, and $T_{\text{tot}} = 1 \text{ h}$. This value equals the smallest detectable signal $(\Delta S/S)_{\text{min}}$ and using Eq. 2 provides an estimate for the minimum mobility that can be detected when evaluating a single data point

$$\mu_{\text{min}} = \left(\frac{\Delta S}{S} \right)_{\text{min}} \frac{2 \sqrt{\epsilon_b}}{Z_0 e n_{2D}} \approx 0.40 \text{ cm}^2/\text{Vs} \quad (8)$$

for $\epsilon_b = 2.8$ and $n_{2D} = 0.92 \times 10^{12} \text{ cm}^{-2}$. Measurements on several organic semiconductors have shown that the practical limit for the lowest detectable mobility is $\mu_{\text{min}} \approx 1 \text{ cm}^2/\text{Vs}$. This agrees well with the mobility of $\mu = 1.5 \text{ cm}^2/\text{Vs}$, which was evaluated for DNNT.

Are the mobilities deduced from THz electromodulation experiments reliable? Carrier mobilities obtained by conventional conductance measurements result from absolute measurements of quantities, as for instance of the current that flows through the FET's channel. In contrast, THz mobilities are deduced from the relative differential transmission $\Delta S/S$, which makes them very reliable. The only uncertainty is the injected charge density, which can be deduced with high precision from the capacitance of the device and from the thresholds of the gate voltages shown in Fig. 5.

Long-time fluctuations of the laser system appear to be a limiting factor. Furthermore, at such small mobilities, the diffusive mean free path of the charge carriers may be smaller than the unit cell of the semiconductor lattice and the Ioffe-Regel criterion prohibits the application of Drude theory [53]. Altogether the minimum detectable mobility of $\mu \approx 1 \text{ cm}^2/\text{Vs}$ shows that the technique can be applied to many molecular and polymeric semiconductors.

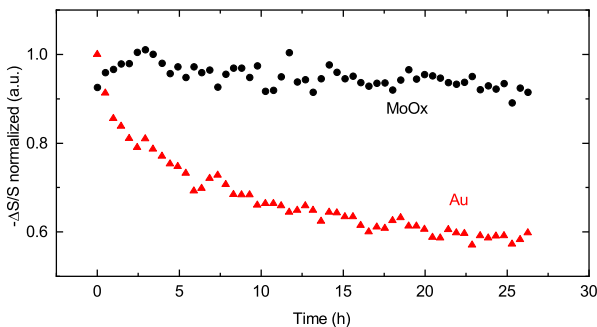


Fig. 9 Decay of the relative differential transmission signal $-\Delta S/S$ with time of a C8-BTBT-C8 device. The red triangles and black circles show data recorded on structures with a Au/Cr injection layer and with a MoO_x/Cr injection layer, respectively

Integration times of several hours, however, require sufficient stability of the investigated devices. The devices' longevity is strongly limited by extrinsic factors. Works on field-effect transistors have shown that indiffusion of water [54, 55] and oxygen [56, 57] reduces device performance, presumably because of trap formation. Two measures help avoiding such impurities: (i) During device fabrication, contaminating the layer surfaces should be avoided. (ii) After device fabrication, the structures should be coated with a protective layer, such as parylene N, which hinders indiffusion of contaminants from the environment.

Another limiting factor is ion migration within the multilayer structure, as this process can rapidly deteriorate the device. We found that gold ions are transported by the electric field from the injection contact toward the channel region [58]. According to Eq. 1, the resulting polarization reduces the number of mobile charges. In structures that contain Au injection layers, $-\Delta S/S$ decreases within few hours, as shown in Fig. 9 because of the reduction of the density of free holes. Much more stable is the usage of MoO_x/Cr injection layers. Such devices have strongly increased lifetimes, as shown in Fig. 9. These results demonstrate that THz electromodulation spectroscopy is also suited for characterizing extrinsic processes that limit the performance of future organic FETs.

The application of THz electromodulation spectroscopy is not limited to the characterization of molecular semiconductors. Attractive is, for instance, its application to polycrystalline and nanocrystalline inorganic semiconductors. In such materials, grain boundaries, traps, and local screening also impact on macroscopic charge transport [59, 60], which makes it difficult to conclude from classical conductance measurements on intrinsic transport properties. Of particular interest may be the application to polymeric semiconductors and blends of polymeric and molecular semiconductors, because of their enormous potential in organic electronics and photovoltaics [61, 62]. Although most amorphous polymers reveal mobilities far below $1 \text{ cm}^2/\text{Vs}$, many works have shown that several semiconducting polymers form composites of a crystalline phase embedded within an disordered phase [63–65]. Here, THz electromodulation spectroscopy may provide insights into the charge transport within those nano-crystallites, which are expected to have much larger mobilities than the surrounding amorphous phase.

6 Conclusion

Terahertz electromodulation spectroscopy provides access to the local properties of electrical transport in thin-film devices of organic semiconductors. The technique can be applied for probing the conductivity of charge carriers having mobilities exceeding $1 \text{ cm}^2/\text{Vs}$. One advantage of the technique is that a relative differential signal is measured, which allows for the deduction of conductivities independent of external factors, such as contact resistances or device geometries. Data evaluation in the frequency domain shows that the charge carriers in molecular semiconductors can be described by a Drude gas with mobilities of about $10 \text{ cm}^2/\text{Vs}$. Besides the determination of charge transport properties, the technique is suited for accessing the impact of

external factors onto device performance, such as degradation due to ion migration from the devices' contacts into the organic semiconductor.

Acknowledgements The authors thank Y. Geerts from Université Libre de Bruxelles for supplying the C₁₂-BTBT-C₁₂ as well as Philipp Altpeter and Christian Obermayer for the technical support.

Author Contribution P. R. and R. K. wrote the manuscript. P. R. measured the data of Figs. 3, 5, 6, and 9. All authors reviewed the manuscript.

Funding Open Access funding enabled and organized by Projekt DEAL. This research was funded by the Deutsche Forschungsgemeinschaft (DFG, German Research Foundation), contract KE 516/11-1.

Data Availability The data that support the findings of this study are available from the corresponding author upon reasonable request.

Declarations

Competing Interests The authors declare no competing interests.

Open Access This article is licensed under a Creative Commons Attribution 4.0 International License, which permits use, sharing, adaptation, distribution and reproduction in any medium or format, as long as you give appropriate credit to the original author(s) and the source, provide a link to the Creative Commons licence, and indicate if changes were made. The images or other third party material in this article are included in the article's Creative Commons licence, unless indicated otherwise in a credit line to the material. If material is not included in the article's Creative Commons licence and your intended use is not permitted by statutory regulation or exceeds the permitted use, you will need to obtain permission directly from the copyright holder. To view a copy of this licence, visit <http://creativecommons.org/licenses/by/4.0/>.

References

1. D.K. Schroder, *Semiconductor Material and Device Characterization* (Wiley - IEEE Press, 2006).
2. X. Guo, Y. Xu, S. Ogier, T.N. Ng, M. Caironi, A. Perinot, L. Li, J. Zhao, W. Tang, R.A. Sporea, A. Nejm, J. Carrabina, P. Cain, F. Yan, *IEEE Trans. Electr. Dev.* **64**, 1906 (2017). <https://doi.org/10.1109/ted.2017.2677086>.
3. T. Someya, Z. Bao, G.G. Malliaras, *Nature* **540**, 379 (2016). <https://doi.org/10.1038/nature21004>.
4. J. Rivnay, S. Inal, A. Salleo, R.M. Owens, M. Berggren, G.G. Malliaras, *Nat. Rev. Mater.* **3**, 17086 (2018). <https://doi.org/10.1038/natrevmats.2017.86>.
5. K. Liu, B. Ouyang, X. Guo, Y. Guo, Y. Liu, *npj Flex. Electron.* **6**, 1 (2022).
6. G. Schweicher, G. Garbay, R. Jouclas, F. Vibert, F. Devaux, Y.H. Geerts, *Adv. Mater.* **32**, 1905909 (2020).
7. C. Rolin, E. Kang, J.H. Lee, G. Borghs, P. Heremans, J. Genoe, *Nat. Commun.* **8**, 14975 (2017).
8. S. Jiang, J. Qian, Q. Wang, Y. Duan, J. Guo, B. Zhang, H. Sun, X. Wang, C. Liu, Y. Shi, Y. Li, *Adv. Electr. Mater.* **6**, 2000136 (2020).
9. V. Podzorov, E. Menard, J.A. Rogers, M.E. Gershenson, *Phys. Rev. Lett.* **95**, 226601 (2005).
10. J.F. Chang, T. Sakanoue, Y. Olivier, T. Uemura, M.B. Dufourg-Madec, S.G. Yeates, J. Cornil, J. Takeya, A. Troisi, H. Sirringhaus, *Phys. Rev. Lett.* **107**, 066601 (2011).
11. W. Warta, N. Karl, *Phys. Rev. B* **32**, 1172 (1985).
12. N. Karl, K.H. Kraft, J. Marktanner, M. Münch, F. Schatz, R. Stehle, H.M. Uhde, *J. Vac. Sci. Techn. A* **17**, 2318 (1999).
13. E.G. Bittle, J.I. Basham, T.N. Jackson, O.D. Jurchescu, D.J. Gundlach, *Nat. Commun.* **7**, 10908 (2016).
14. H.H. Choi, K. Cho, C.D. Frisbie, H. Sirringhaus, V. Podzorov, *Nat. Mat.* **17**, 2 (2018). <https://doi.org/10.1038/nmat5035>.
15. P.U. Jepsen, D.G. Cooke, M. Koch, *Laser Photonics Rev.* **5**, 124 (2011).
16. M. van Exter, D. Grischkowsky, *Appl. Phys. Lett.* **56**, 1694 (1990).

17. N. Katzenellenbogen, D. Grischkowsky, Appl. Phys. Lett. **61**, 840 (1992).
18. G. Horowitz, in *Organic Electronics*, ed. by H. Klauk (WILEY-VCH, 2006).
19. L. Fekete, P. Kuzel, H. Nemeč, F. Kadlec, A. Dejneka, J. Stuchlik, A. Fejfar, Phys. Rev. B **79**, 115306 (2009).
20. J.B. Baxter, C.A. Schmuttenmaer, J. Phys. Chem. B **110**, 25229 (2006).
21. E. Hendry, M. Koeberg, J.M. Schins, H.K. Nienhuys, V. Sundström, L.D.A. Siebbeles, M. Bonn, Phys. Rev. B **71**, 125201 (2005).
22. E. Hendry, F. Wang, J. Shan, T.F. Heinz, M. Bonn, Phys. Rev. B **69**, 081101(R) (2004).
23. S. Seki, A. Saeki, T. Sakurai, D. Sakamaki, Phys. Chem. Chem. Phys. **16**, 11093 (2014).
24. W. Choi, Y. Tsutsui, T. Sakurai, S. Seki, Appl. Phys. Lett. **110**, 153303 (2017).
25. D. Mittleman, *Sensing with Terahertz Radiation* (Springer, Berlin, 2002).
26. C.A. Schmuttenmaer, Chem. Rev. **104**, 1759 (2004).
27. P.R. Smith, D.H. Auston, M.C. Nuss, IEEE Journal of Quantum Electronics **24**(2), 255 (1988). <https://doi.org/10.1109/3.121>.
28. C. Fattinger, D. Grischkowsky, Appl. Phys. Lett. **54**, 490 (1989).
29. H. Harde, D. Grischkowsky, J. Opt. Soc. Am. B **8**, 1642 (1991).
30. R.H. Jacobsen, K. Birkelund, T. Holst, P.U. Jepsen, S.R. Keiding, J. Appl. Phys. **79**, 2649 (1996).
31. R. Kersting, K. Unterrainer, G. Strasser, H.F. Kauffmann, E. Gornik, Phys. Rev. Lett. **79**, 3038 (1997).
32. S.E. Ralph, D. Grischkowsky, Appl. Phys. Lett. **60**, 1070 (1992).
33. J.N. Heyman, R. Kersting, K. Unterrainer, Appl. Phys. Lett. **72**, 644 (1998).
34. Q. Wu, X.C. Zhang, Appl. Phys. Lett. **67**, 3523 (1995).
35. Q. Wu, M. Litz, X.C. Zhang, Appl. Phys. Lett. **68**, 2924 (1996).
36. A. Dreyhaupt, S. Winnerl, T. Dekorsy, M. Helm, Phys. Lett. **86**, 121114 (2005).
37. D. Sailer, A. Borschlegl, R. Kersting, Appl. Phys. Lett. **117**, 083301 (2020).
38. T. Yamamoto, K. Takimiya, J. Am. Chem. Soc. **129**, 2224 (2007).
39. P. Xie, T. Liu, J. Sun, J. Yang, Adv. Func. Mater. **32**, 2200843 (2022).
40. D. Kumaki, T. Umeda, S. Tokito, Appl. Phys. Lett. **92**, 013301 (2008).
41. M.T. Greiner, Z.H. Lu, NPG Asia Materials **5**, e55 (2013).
42. J.B. Fortin, T.M. Lu, *Chemical Vapor Deposition Polymerization: The Growth and Properties of Polyene Thin Films* (Kluwer Academic Publishers, Boston, Dordrecht, New York, London, 2004).
43. J.T.E. Quinn, J. Zhu, X. Li, J. Wang, Y. Li, J. Mater. Chemistry C **5**, 8654 (2017). <https://doi.org/10.1039/c7tc01680h>.
44. R.E. Glover, M. Tinkham, Phys. Rev. **108**, 243 (1957).
45. S. Funk, G. Acuna, M. Handloser, R. Kersting, Opt. Expr. **17**, 17450 (2009).
46. J. Neu, K.P. Regan, J.R. Swierk, C.A. Schmuttenmaer, Appl. Phys. Lett. **113**, 233901 (2018).
47. C. Grigoriadis, C. Niebel, C. Ruzie, Y.H. Geerts, G. Floudas, J. Phys. Chem. B **118**, 1443 (2014).
48. T.R. Arend, A. Wimmer, G. Schweicher, B. Chattopadhyay, Y.H. Geerts, R. Kersting, J. Phys. Chem. Lett. **8**, 5444 (2017).
49. P. Yeh, *Optical waves in layered media* (Wiley, 2005).
50. M. Dressel, G. Grüner, *Electrodynamics of Solids* (Cambridge University Press, 2002).
51. H. Altan, F. Huang, J.F. Federici, A. Lan, H. Grebel, J. Appl. Phys. **96**, 6685 (2004).
52. S.G. Engelbrecht, M. Prinz, T.R. Arend, R. Kersting, Appl. Phys. Lett. **105**, 012101 (2014).
53. N.F. Mott, E.A. Davis, *Electronic processes in non-crystalline materials* (Clarendon Press, 1979).
54. C. Goldmann, D.J. Gundlach, B. Batlogg, Appl. Phys. Lett. **88**, 063501 (2006).
55. A. Tamayo, T. Salzillo, M. Mas-Torrent, Adv. Mater. Interf. **9**, 2101679 (2022).
56. A. Benor, A. Hoppe, V. Wagner, D. Knipp, Org. Electr. **8**, 749 (2007).
57. T. Hallam, C.M. Duffy, T. Minakata, M. Ando, H. Sirringhaus, Nanotechn. **20**, 025203 (2009).
58. P. Riederer, M. Bouraoui, R. Kersting, Appl. Phys. Lett. **120**, 243503 (2022).
59. S.G. Engelbrecht, L. De Angelis, M. Tönnies, R. Kersting, Appl. Phys. A **113**, 641 (2013).
60. S.G. Engelbrecht, T.R. Arend, T. Zhu, M.J. Kappers, R. Kersting, Appl. Phys. Lett. **106**, 092107 (2015).
61. C. Mueller, T.A.M. Ferenczi, M. Capoy-Quiles, J.M. Frost, D.D.C. Bradley, P. Smith, N. Stingelin-Stutzmann, J. Nelson, Adv. Mat. **20**, 3510 (2008).
62. K.J. Baeg, M. Caironi, Y.Y. Noh, Adv. Mater. **25**, 4210 (2013).
63. R. Noriega, J. Rivnay, K. Vandewal, F.P.V. Koch, N. Stingelin, P. Smith, M.F. Toney, A. Salleo, Nature Mat. **12**, 1038 (2013).

64. X. Xue, G. Chandler, X. Zhang, R.J. Kline, Z. Fei, M. Heeney, P.J. Diemer, O.D. Jurchescu, B.T. O'Connor, *ACS Appl. Mater. Interfaces* **7**, 26726 (2015).
65. Y. Lei, P. Deng, M. Lin, X. Zheng, F. Zhu, B.S. Ong, *Adv. Mater.* **28**, 6687 (2016).

Publisher's Note Springer Nature remains neutral with regard to jurisdictional claims in published maps and institutional affiliations.